On the origin of Saturn's outer auroral emission

Denis Grodent,[1] Aikaterini Radioti,[1] Bertrand Bonfond,[1] and Jean-Claude Gérard[1]

Received 14 September 2009; revised 5 January 2010; accepted 8 January 2010; published 18 August 2010.

[1] Ultraviolet Hubble Space Telescope images reveal a faint but distinct auroral emission equatorward of the main ring of emission of Saturn's southern polar region. This outer auroral emission is only visible near the nightside limb for the strongly tilted viewing geometry achieved in January 2004. We model the limb-brightening amplification of this emission, and we show that the observations are compatible with an ~7° wide emission ring approximately centered on the 67°S parallel. The 1.7 kR brightness of this emission requires an injected electron energy flux of ~0.3 mW m^{-2}. The outer auroral emission maps to a region of the equatorial plane between 4 and 11 R_S. We suggest that a population of suprathermal electrons observed by Cassini can provide more than the required energy flux without the need for field-aligned acceleration. This auroral UV emission may also be associated with energetic neutral oxygen and hydrogen atoms originating from the energetic protons and O^+ of magnetosphere and/or with a secondary infrared auroral oval.

Citation: Grodent, D., A. Radioti, B. Bonfond, and J.-C. Gérard (2010), On the origin of Saturn's outer auroral emission, *J. Geophys. Res.*, *115*, A08219, doi:10.1029/2009JA014901.

1. Introduction

[2] During January 2004, 17 Hubble Space Telescope (HST) orbits were devoted to the observation of Saturn's southern auroral emissions with the Space Telescope Imaging Spectrograph (STIS). A total of 68 far ultraviolet (FUV) images were collected, spanning a 4 week period during which the Cassini spacecraft was approaching Saturn's magnetosphere and detected a series of solar wind perturbations propagating toward Saturn. These images exhibit a complex and changing auroral morphology. This large number of images made it possible to draw a statistical picture of Saturn's southern auroral morphology which was later confirmed by recent HST campaigns using the Advanced Camera for Surveys (ACS). Among the different components of the auroral morphology, one is so faint that it can only be observed under very specific viewing geometries. This auroral feature, which *Grodent et al.* [2005] named the "outer emission," appears as a permanent secondary arc equatorward of the main emission. It is revealed by limb brightening of the optically thin H_2 auroral emission and therefore, can only be detected in the nightside sector between 0600 LT and 1800 LT, through midnight. In January 2004, the conditions were met to observe this emission; the sub-Earth latitude reached a value of 26°S, a geometry which will not repeat before 2032 (2017 for the northern hemisphere). This large tilt of Saturn's ring plane implies that the nightside portion of the southern auroral emission region comes into view below the south pole, very close to the planetary limb. During this period, the Sun achieved one full rotation and the solar wind that reached Saturn exhibited various states, ranging from quiet periods to very active ones characterized by major compression regions. Several studies [*Grodent et al.*, 2005; *Clarke et al.*, 2005, 2009; *Crary et al.*, 2005] have demonstrated that solar wind conditions influence the auroral morphology. In particular, the size of the main ring of auroral emission appears to be anticorrelated with solar wind ram pressure. This behavior suggests that, like on Earth, a compression of the magnetosphere may lead to rapid tail reconnection and a reduction of the open field region by closure of magnetic flux [*Cowley et al.*, 2005]. This would then favor the theoretical model of *Cowley and Bunce* [2003], and more recently of *Bunce et al.* [2008a], who proposed that the main auroral emission of Saturn results from upward directed field-aligned currents associated with the shear in rotational flow across the open-closed field line boundary, contrary to Jupiter where the main auroral emission appears to be associated with the process of corotation enforcement.

[3] On 26 January 2004 the aurora contracted in a small region of the dawn sector. This dramatic change was attributed to the arrival of a strong solar wind shock on 25 January. Following Saturn's plasma flows and currents model described by *Cowley et al.* [2004], *Grodent et al.* [2005] suggested that the resulting magnetospheric compression induced an interval of rapid reconnection in the nightside tail which closed a substantial fraction of the preexisting open flux and led to a generalized contraction of the auroral emission region. As a result of this contraction, the main ring of emission cleared the dusk and nightside sectors revealing an extended fainter, permanent band of emission at low latitude. Figure 1a displays a polar projection, fixed with respect to the Sun (dawn on the left and midnight at the top), of the sum of the two "clear" STIS images (Figure 1c) of Saturn's southern hemisphere which were taken during

[1]LPAP, Institut d'Astrophysique et de Géophysique, Université de Liège, Liège, Belgium.

0148-0227/10/2009JA014901

this unusual event. The bright main auroral emissions (blue tones) are concentrated in the dawnside hemi-disk spreading between the pole and the 70°S parallel. The more than 10 times fainter outer auroral emission (red tones) appears as a completely distinct feature at latitudes equatorward of 70°S. This emission exceeds the background emission only in the region mapping to the nightside sector of the magnetosphere, that is, from 1800 LT to 0600 LT through midnight. *Grodent et al.* [2005] suggested that the outer emission is common to the entire data set. They proposed that this tenuous emission scarcely detaches from the background emission by a few kilorayleighs (kR). Its morphology and mean brightness remain almost constant over the whole January 2004 data set, suggesting that it is produced by a mechanism different from the rest of the auroral emission. The former analysis did not go further in estimating the auroral brightness and no attempt was made to link it with a magnetospheric source.

[4] In the present study, we provide an accurate determination of the limb brightening affecting the apparent brightness and a verification of the existence of the outer auroral emission as well as possible sources of energetic electrons giving rise to this localized equatorward emission.

2. Observations

[5] The observations were described in detail by *Grodent et al.* [2005]. The images are obtained with the STIS camera on board HST. Half of them were taken while in the shadow of the Earth where geocoronal contamination is lowest. For these images, the 115–170 nm spectral range of the "clear" (no filter) mode was used to capture the auroral H_2 Lyman and Werner bands emission as well as the strong H Lyman-α line. For the other images, taken immediately before and after Earth shadow time, the F25-SrF2 filter was added in order to reject the emission shortward of 125 nm, including the H Lyman-α line. The "clear" images were accumulated for 270 s and the filtered images were obtained in time-tag mode with exposure times varying from 640 s to 740 s. The 68 images were acquired during 17 HST orbits obtained every ~2 days between 8 and 30 January 2004.

[6] As stated above, Figures 1a and 1c illustrate an extreme case during which the morphology of the bright main auroral emission was particularly favorable (contracted) to observe the nightside outer auroral emission. However, this emission is also apparent, to a lesser extent, in all other images.

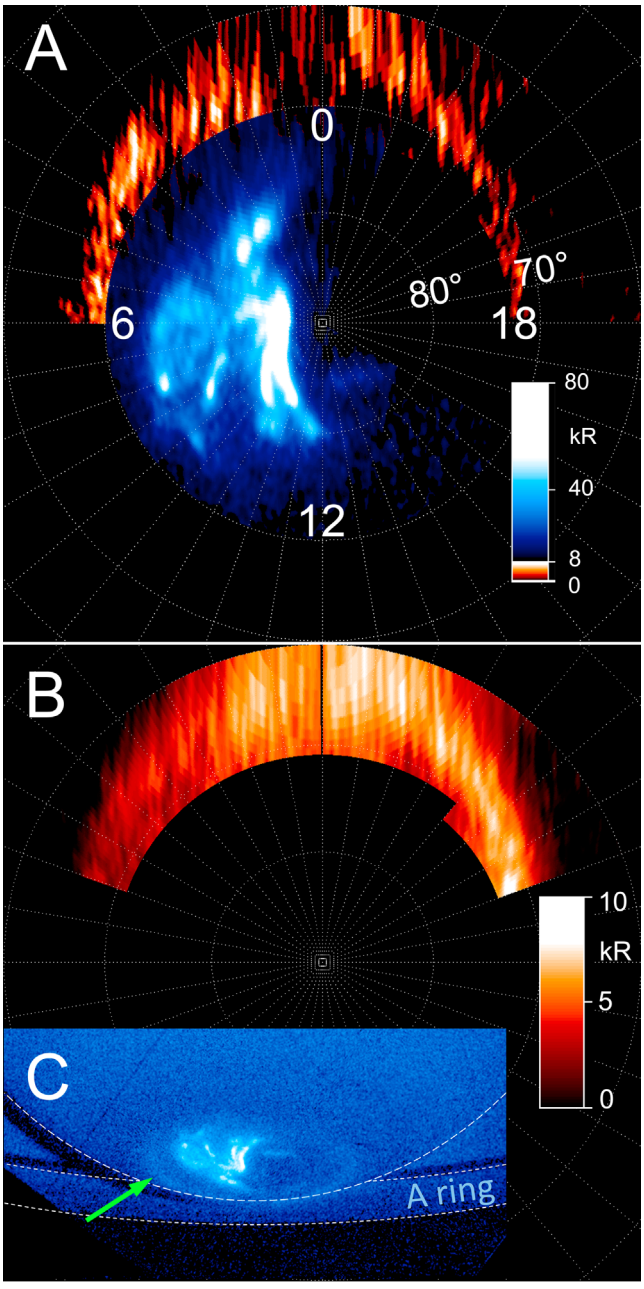

Figure 1. (a) Polar projection, fixed with respect to the Sun (dawn on the left and midnight at the top), of the sum of the two "clear" Space Telescope Imaging Spectrograph (STIS) images of Saturn's southern hemisphere that were taken during the compression event on 26 January 2004. The typical bright main auroral emissions (blue tones) are concentrated in the dawnside hemi-disk spreading between the pole and the 70°S parallel. The more than 10 times fainter outer auroral emission (red tones) appears as a distinct feature at latitudes equatorward of 70°S. This emission exceeds the background emission only in the region mapping to the nightside sector of the magnetosphere. The contrast between the outer emission and the rest of the auroral emission is enhanced by using different color tables (red for the outer emission and blue for the main emission) spanning different portions of the brightness range. The grid is made of 10° spaced meridians and parallels, and the polar projection assumes that the emission is located at 1000 km above the 1 bar pressure level. Local times at 0000, 0600, 1200, and 1800 LT as well as the 70° and 80° southern parallels have been marked on the polar view. (b) Polar projection of the sum of 34 "clear" STIS images obtained from 8 to 30 January 2004. Only the outer auroral emission is displayed. The LT fixed grid is the same as that in Figure 1a. (c) Sum of the two "clear" STIS images of Saturn's southern hemisphere that were taken during the unusual event of 26 January 2004. The polar projection of this sum is displayed in Figure 1a. The green arrow points to the faint outer auroral emission, and the dashed lines show the planetary limb and the A-ring boundaries.

Table 1. Latitudinal Gaussian Width and Central Southern Latitude of the Auroral Intensity as a Function of Latitude for Different Longitude Ranges[a]

LT Longitude Range	FWHM	Central Latitude	Distance
30–35°	7.3°	67°	6 R_S
305–310°	5.5°	70°	9 R_S
340–345°	7.0°	64°	5 R_S
355–360°	12.0°	64°	5 R_S

[a]Local time longitudes are given in degrees from midnight (0° = 0000 LT = midnight, 270° = 1800 LT = dusk). The last column provides the radial distance mapped to the equatorial plane with the magnetic field model described by *Bunce et al.* [2008b]. These values are obtained from the sum of 34 Space Telescope Imaging Spectrograph (STIS) images displayed in Figure 1b. They are roughly compatible with a simple ~7° wide circular emission pattern centered on 67°S. FWHM, full width at half maximum.

[7] Figure 1b shows the polar projection of the sum of 34 "clear" STIS images obtained from 8 to 30 January 2004. Contrary to Figure 1a, only the outer auroral emission is displayed. Again, it forms a roughly circular ~7° wide pattern along the 67°S parallel, although it appears narrower and closer to 70°S at the dawn and dusk edges. More detailed values of width and central latitude are given in Table 1. They are obtained from Gaussian fits of the intensity (displayed in Figure 1b) versus latitude averaged over four representative ranges of local time longitude. There is no definite brightness distribution even though one may argue that the emission is dimmer on the dawn side, but this slight trend contradicts the opposite trend in Figure 1a. The similarity between the extreme and average outer emission morphologies shown in Figures 1a and 1b contrasts with the remarkable change in the brightness distribution of the main emission. *Grodent et al.* [2005] showed that the latitude of the main ring of emission increased by more than 5° at the time of the extreme event illustrated in Figure 1a. No noticeable shift of the outer emission can be measured, even though it lies at lower latitudes where changes should be more pronounced, given the lower magnetic field lines density at lower latitude. This suggests that the mechanism giving rise to the outer emission is much less affected by the solar wind conditions and is likely different from the rest of the emission.

3. Background Emission

[8] The first step to obtain the injected auroral power consists in estimating the background contribution from the planetary disk. Since a substantial portion of the high-altitude auroral emission extends beyond the planetary disk, it is also necessary to estimate the contribution from the A-ring. In order to increase the signal-to-noise ratio (S/N), we add the two "clear" images obtained during the "Earth shadow time" of each HST orbit. Cuts through the planetary disk and ring show that at the edges of the auroral region, (1) the disk background is essentially constant over the auroral zone, and (2) the contribution from the A-ring is, at most, similar to the disk. Accordingly, we manually sample the disk background in two small regions directly adjacent to the outer emission (poleward and equatorward) for each of the 17 summed images of the data set. An average background value is then calculated for each image and subtracted. The average background varies from 6.5 to 9 kR, depending on the residual geocoronal contamination during each HST orbit. The standard deviation of the background emission is estimated in the same regions and shows to vary similarly from 2 to 4 kR.

4. Limb Brightening

[9] The main interest of the present data set stems from the high inclination of Saturn's spin axis. In January 2004, the sub-Earth latitude was about 26°S which brings the nightside southern auroral region into view near the planetary limb. The H_2 auroral FUV emission is optically thin and, as a result, it accumulates along the observer's line of sight. This limb-brightening (LB) effect changes the apparent brightness of the emission and becomes increasingly important as one nears the planetary limb. The planetary disk background observed in the "clear" images, and discussed above, is mainly reflected sunlight longward of 160 nm. It is not affected by limb brightening, it is actually limb darkened as a result of the presence of high-altitude haze, especially in the polar/auroral regions, which produces absorption [*Vincent et al.*, 2000], and therefore it does not increase like the auroral emission toward the limb. As a consequence, limb brightening is able to reveal very faint auroral emissions near the limb (above and below the limb) which otherwise would not exceed the background by more than one standard deviation and could not be detected.

[10] To estimate limb brightening, we use the Chapman function, which gives the ratio of the slant column emission rate to the vertical column emission rate and may be approximated by the secant of the latitude angle. However, this method usually assumes that the emission is uniformly covering a spherical planet and significantly overestimates the effect for a discrete emission shaped like an arc, especially at the planetary limb. In order to estimate the auroral intensity free of limb brightening, we employ the forward simulation described by *Grodent et al.* [1997]. The code was adapted to Saturn's dimensions and viewing geometry. The projection of the auroral outer emission feature on the surface may be simulated with a simple 7° wide ribbon centered on the 67°S (planetocentric) parallel. The input emission distribution in longitude-latitude used in the simulation is displayed on a polar map in Figure 2a. We note that, as discussed in section 2, the actual ribbon of emission slightly deviates from a simple concentric annulus near the dawn and dusk ansae where the brightest emission (dusk) reaches poleward latitudes on the order of 70°S. The model vertical extent of the emission is plotted in Figure 2b. It is uniform over the ribbon and is assumed to follow a Chapman profile, not to be confused with the Chapman function, characterized by an emission peak lying 1000 km above the 1 bar pressure level, and a scale height of 500 km. These values are in full agreement with the measurements and analysis of *Gérard et al.* [2009]. Since *Gustin et al.* [2009] showed that the auroral H_2 spectra of Saturn are generally very weakly absorbed by methane, we did not consider the effect of CH_4 in the simulations.

5. Results

[11] Figure 3 displays the simulated outer emission obtained with the above parameters and provides a general view

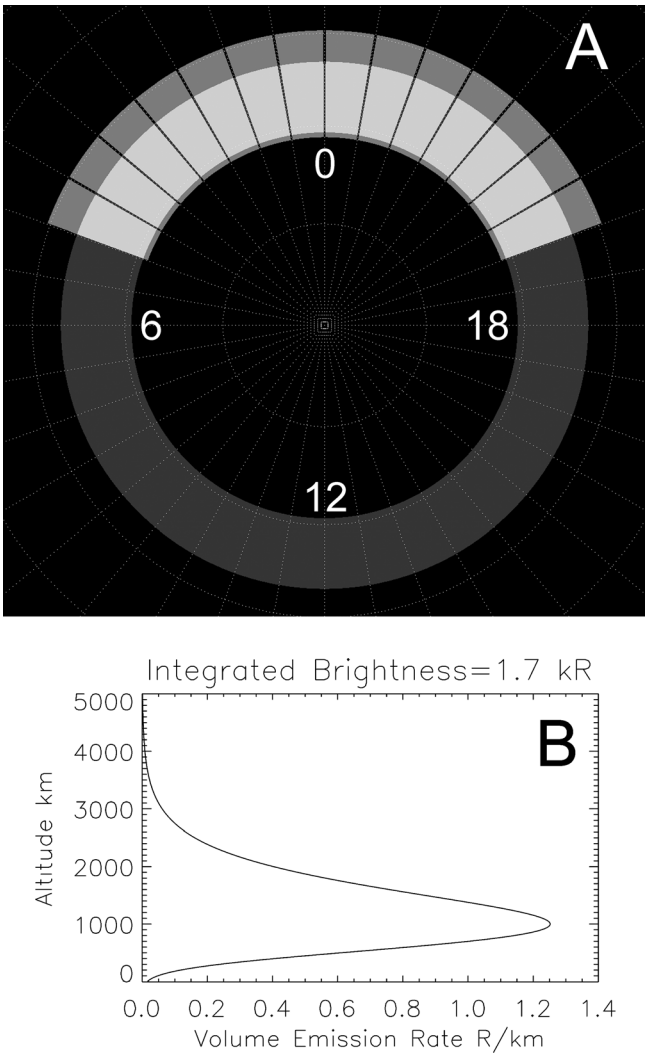

Figure 2. (a) Polar view of the input emission distribution in longitude-latitude used in the simulation of the outer auroral emission (dark gray). The input emission consists of a simple distribution uniformly filling a 7° wide ribbon centered on the 67°S parallel. The LT fixed grid is the same as that in Figure 1, and the emission distribution may be directly compared with that of the observed one. The 14 highlighted sectors (light gray) around midnight (0000 LT) correspond to 10° longitude sectors from 60° to 71° of southern latitude at an altitude of 1000 km. They define surfaces of equal area in which we evaluate the brightness in the set of HST images and in the simulated view of the outer emission. Local times at 0000, 0600, 1200, and 1800 LT have been marked on the polar map. (b) Vertical distribution of the input emission, which follows a Chapman profile characterized by an emission peak lying 1000 km above the 1 bar pressure level and a scale height of 500 km. The height-integrated brightness is 1.7 kR.

of the LB effect. The planetary grid assumes a tilted ellipsoid 1000 km larger than Saturn in order to more adequately map the auroral emission. For Saturn, we use the recommended flattening value of 0.098 [*Seidelmann et al.*, 2007] corresponding to equatorial and polar radii of 60,268 and 54,364 km, respectively. In Figure 3 the boundaries of the A-ring and B-ring, separated by the Cassini division, are positioned at the proper distances (assuming transparent planet). An additional trace within the A-ring (126,000 km) marks a sudden change in the ring UV reflectivity [*Nicholson et al.*, 2008]. The limb brightening ranges from a multiplying factor of ~1.3 near noon to ~5 above the limb, reaching a value of ~3 near the dawn and dusk ansae. Accordingly, with an average background standard deviation of 3 kR, the LB-free auroral emission near noon must be larger than 2 kR in order to be detected. At the nightside limb it must be at least 600 R, and near the dawn and dusk ansae the minimum detectable brightness is ~1 kR.

[12] The 14 highlighted regions on Figure 2a correspond to 10° longitude sectors from 60° to 71° of southern latitude, slightly larger than the outer auroral ribbon, at an altitude of 1000 km. They define surfaces of equal area on the planet (~4.3 10^7 km^2) in which we evaluate the brightness in the set of HST images and in the simulated view of the outer emission. Setting the altitude of these sectors to 1000 km and their latitude range to 11° allows us to pick most of the auroral emission above the 0 km limb. Similarly, the upper latitude boundary of the longitude sectors is the result of a trade-off between the need to select the majority of the high-latitude outer emission and the exclusion of the contribution from the main ring of auroral emission. This technical limitation leads us to consider the maximum brightness in each sector, rather than the average brightness, the latter of which strongly depends on the efficiency with which each longitude sector encompasses the auroral region of interest.

[13] Figure 4 plots the observed and simulated maximum brightness in the different LT longitude sectors highlighted in Figure 2a. The diamonds in each column correspond to the 17 HST orbits under consideration and illustrate the variability of the emission. Data points corresponding to the compression event illustrated in Figure 1a are highlighted with stars. The first column is the first longitude sector sampling the

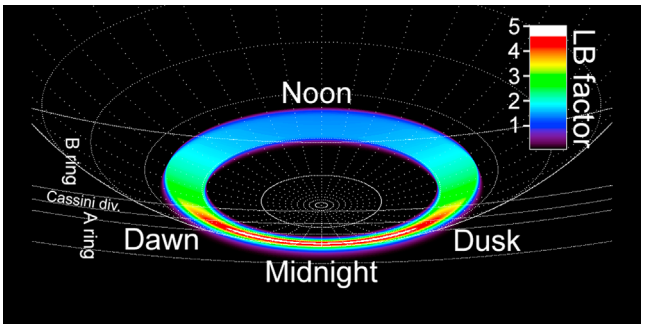

Figure 3. Simulated outer auroral emission obtained with the parameters inferred from Figure 1b and presented in Figure 2, which provides a general view of the limb-brightening effect. The planetary grid assumes a tilted ellipsoid 1000 km larger than Saturn. The boundaries of the A-ring and B-ring, separated by the Cassini division, are positioned at the proper distances (assuming transparent planet). An additional trace within the A-ring (126,000 km) marks a sudden change in the ring UV reflectivity. The limb-brightening factor ranges from ~1.3 near noon to ~5 above the limb, reaching a value of ~3 near the dawn and dusk ansae.

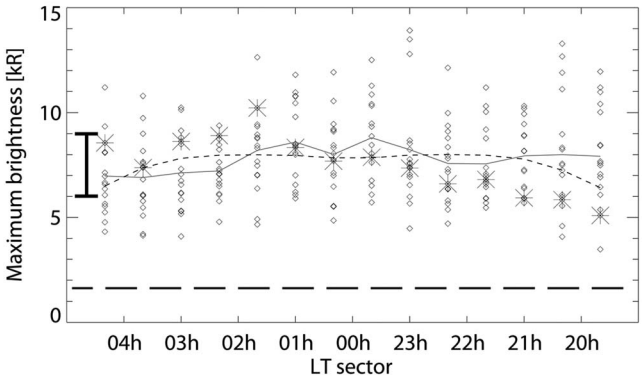

Figure 4. Maximum brightness (kR) in the 14 sectors highlighted in Figure 2a. The diamonds in each column correspond to the 17 HST orbits that we consider and illustrate the variability of the emission. The first column is the first longitude sector sampling the dawn ansa (near 0400 LT) of the outer aurora, and the last column samples the dusk ansa (near 2000 LT). Data points corresponding to the compression event illustrated in Figures 1a and 1c are highlighted with stars. The solid line depicts the average value of the maximum brightness as a function of the LT sector. This line is relatively flat with an average value of ~8 kR. The dashed line represents the maximum brightness, which is inferred from the simulated image (Figure 3) assuming a uniform limb-brightening-free emission of 1.7 kR represented by the thick dashed line. The vertical thick bar on the left corresponds to the level of statistical fluctuation of the signal ($1\sigma \approx 3$ kR).

dawn ansa (after 0400 LT) of the outer aurora and the last column samples the dusk ansa (before 2000 LT). The solid line joins data points which correspond to the average over the 17 HST orbits of the maximum observed values for each longitude sector displayed in Figure 2a. This line is relatively flat with an average value of ~8 kR; it shows slightly smaller values near the ansae of the outer emission. The simulated maximum brightness's are represented by a dashed line in Figure 4. They were obtained by assuming that the height integrated Chapman profile displayed in Figure 2b is 1.7 kR for all latitudes and longitudes enclosed in the circular model ribbon represented in Figure 2a. Like the observed values, their LT distribution is saturating at ~8 kR and slightly decreasing near the ansae. It might then be stated that the observed maximum brightness distribution is best fit with a model outer emission of 1.7 kR unaffected by limb effects. This retrieved value of the LB-free brightness is compatible with the outer auroral brightness distribution observed in Figure 1b. It is less than 10% of the main auroral brightness which is usually varying from 10 to 100 kR [e.g., *Grodent et al.*, 2005]. Moreover, it is too small to give rise to measurable emission in the dayside portion of the outer aurora and produces an apparent brightness in the region mapping to the nightside as large as 8.5 kR (5 × 1.7 kR), that is, 2 to 3 standard deviations above the background emission. As a consequence, it cannot be ascertained whether the outer emission is present all around the pole or if it is limited to the nightside region of the aurora. For the data set used here the outer emission is also too faint to distinguish substructures that would enable us to determine if the outer emission is fixed in local time or if it is rotating with the planet.

[14] The scattering of the observed maximum brightness (vertical distribution of the diamonds in Figure 4) is of order of ±2.5 kR. It adds to the statistical background fluctuations (1σ ~3 kR) to provide a rough estimate of the upper limit to the accuracy of the best fit value of 2.5 + 3 = 5.5 kR which scales down to 1.2 kR, if we take into account the fact that a LB-free emission gives rise to a maximum brightness of 8 kR. The LB-free brightness is thus 1.7 kR ± 1.2 kR meaning that, for practical purposes, this value is valid within a factor of ~2. During the compression event observed on 26 January 2004 (Figure 1) the brightness of the main emission dramatically increased by at least a factor of two. However, the highlighted data points in Figure 4 show that on that day the outer emission does not significantly depart from the rest of the data set, instead it remains to the average value. This suggests again that, contrarily to the main emission, the outer auroral emission is likely produced by a mechanism that does not notably react to solar wind variations.

6. Interpretation and Discussion

6.1. Mapping and Energy Flux Estimate

[15] According to the magnetic field model of Saturn's magnetosphere described by *Bunce et al.* [2008b], a 7° wide outer auroral region centered on 67°S latitude roughly maps to the equatorial plane at radial distances ranging from ~4 R_S (1 Saturn radius = 1 R_S = 60,268 km) to ~11 R_S. This region of the equatorial plane roughly corresponds to the E-ring and may, more appropriately, be identified with the inner plasmasphere. During Cassini's initial orbit, the Cassini plasma spectrometer (CAPS) detected an electron population characterized by a bi-Maxwellian velocity distribution [*Young et al.*, 2005]. This population, bound to the inner plasmasphere (between ~4 and 9 R_S), consists of a hot (keV) tenuous component and a cold (eV) dense component. These results were recently confirmed by *Schippers et al.* [2008] and *Lewis et al.* [2008], although they somewhat extend the magnetospheric region of suprathermal electrons to larger distances, starting from 7 R_S to beyond 10 R_S. Like *Cowley and Bunce* [2003], we consider that only the warm electron population is able to reach Saturn's ionosphere since the cold population remains trapped by the cool ions near the equatorial plane where they maintain charge neutrality. From the detailed results presented by *Schippers et al.* [2008], we estimate that the suprathermal electron population thermal energy and density are $W_{th} \approx 1$ keV and $N \approx 10^5$ m^{-3}, respectively, in the inner plasmasphere, with a pronounced peak near 9 R_S (mapping to 70°S) for both W_{th} and N. These parameters are injected in equations (20) and (21) of *Cowley and Bunce* [2003], using their assumption on the full loss cone distribution, to evaluate the maximum current density that can be carried to Saturn's ionosphere by these warm electrons without field-aligned acceleration ($j_{//i0}$) and the corresponding precipitated electron energy flux (E_{f0}). We then obtain $j_{//i0}$ = 85 nA m^{-2} and E_{f0} = 0.17 mW m^{-2}. Assuming that it is necessary to inject 10 mW m^{-2} in order to obtain 1 mW m^{-2} of auroral UV emission [*Grodent et al.*, 2001], and considering that the energy of one FUV photon is ~10 eV then an emission brightness of 1.7 kR requires the injection of ~0.27 mW m^{-2}

in the southern ionosphere. This is roughly comparable to the energy flux which is available from the hot electron population of the inner plasmasphere (E_{f0}). A more detailed approach, taking into account the energy spectrum of the electrons, suggests that more energy may be available. Indeed, *Schippers et al.* [2008] reported a narrow boundary region near 9 R_S where the pitch angle distribution is rapidly changing from a pancake population to a bidirectional distribution beyond 9 R_S. *Tomás et al.* [2004] and *Radioti et al.* [2009] observed a similar pitch angle transition in the magnetosphere of Jupiter indicative of electron diffusion. In particular, they showed that this transition region is concurrent with observed whistler mode waves that are able to scatter the electrons into the loss cone and trigger auroral emissions. This region directly maps to a diffuse secondary auroral oval, equatorward of and fainter than the main auroral oval of Jupiter, thus showing some morphological similarities with the outer auroral emission at Saturn. They estimated that the available energy flux is sufficient to sustain the brightness of this secondary auroral oval. We follow the same procedure as that of *Radioti et al.* [2009], and we assume strong diffusion (a full loss cone). This assumption may be justified, at least in the pitch angle transition region, by the presence of whistler waves emissions originating from the E-ring region [*Scarf et al.*, 1983]. We use the energy distribution at 9 R_S given by *Schippers et al.* [2008] to derive the precipitating energy flux. The electrons with a thermal energy between 0.2 and 3 keV provide an energy flux of ~0.27 mW m^{-2}, which is exactly equal to our previous estimate (this perfect agreement is purely fortuitous, given the number of approximations which were used to derive these values). However, in addition, electrons with energy >3 keV appear to supply more than 2 mW m^{-2}. This suggests that the suprathermal electron component of the inner plasmasphere, carries enough energy to produce the observed outer auroral emission in both hemispheres, without field-aligned acceleration.

6.2. Energetic Neutral Atoms

[16] *Carbary et al.* [2008] described emissions of magnetospheric energetic neutral oxygen and hydrogen atoms (ENA) observed with the MIMI instrument onboard Cassini. The magnetic mapping of these ENA emissions places them equatorward of the main auroral emission where they form a distinct feature. These emissions result from charge exchange between hot ions and cold neutrals; they therefore are representative of a localized hot plasma population as reported by *Sergis et al.* [2007]. The relation between ENA generation from magnetically trapped hot ions and precipitation of auroral electrons is not straightforward. It was speculated that azimuthal ring current pressure gradients resulting from localized enhanced ion intensities generate field-aligned current structures that may be responsible for the production of auroral emissions [*Mitchell et al.*, 2009]. When averaged over several rotational periods and projected onto the equatorial plane, these emissions form toroidal distributions nearly concentric with the planet and peaking just before midnight. The averaged and projected ENA emissions are located at a mean distance of ~11 R_S and ~8 R_S of the spin axis, respectively. These distances fall in the upper half of the mapped outer auroral emission range (4–11 R_S) and imply a possible relation between these hot populations and associated ENAs and the outer auroral UV emission, although large mapping inaccuracies on the source location of the ENAs and on the outer emission may challenge this association. However, it should be noted that Cassini in situ measurements of the energetic O^+ and H^+ population [*Sergis et al.*, 2007], which is the source of ENA emissions, suggest that particle pressure is enhanced in the region between dipole L values of L = 8 and L = 14. This range of radial distances approximately overlaps the mapped outer auroral emission in the range 8–11 R_S and corresponds to radial distances where the pressure is peaking.

[17] In the case of the Earth, *Hubert et al.* [2001] showed that auroral diffuse emission similarly appears equatorward of the main electron-excited auroral arc in the premidnight sector. This diffuse emission results mainly from the precipitation of protons which may have undergone strong pitch angle diffusion as a result of the presence of a thin current sheet in the nightside part of the magnetosphere which is stretching the field lines [e.g., *Sergeev et al.*, 1983]. The presence of a variable ring current at Saturn [*Sergis et al.*, 2007] implies magnetic field lines stretching and, if sufficiently important, may provide a possible mechanism for scattering hot H^+ into the loss cone. Accordingly, one cannot discard the possibility that the outer auroral emission results, at least partially, from proton precipitation. The present HST data set does not permit one to discriminate between proton and electron precipitation, the former of which should be characterized by stronger Doppler-shifted Ly-α line emission. Analysis of Cassini/UVIS spectral images of Saturn's auroral emission might provide insight to the origin of this faint outer emission.

6.3. Infrared Secondary Oval

[18] *Stallard et al.* [2008] reported the presence of a secondary auroral oval equatorward of the main oval in Saturn's infrared thermal auroral emission of H_3^+. This auroral feature, to some extent, resembles the ultraviolet outer auroral emission described here. It appears as a residual intensity in spectral slit images of Saturn's southern auroral region following subtraction of a modeled main auroral oval intensity. Its brightness is peaking at about 20% of the main auroral oval and its associated line-of-sight velocity shows that this emission is significantly subcorotating. *Stallard et al.* [2008] suggested that the connection between the secondary oval and its subcorotating nature in the ionosphere implies that corotation breakdown within the magnetospheric plasma could give rise to a system of field-aligned currents (FAC) strong enough to power the secondary infrared auroral oval, similar to the Jovian main auroral emission but scaled down by 2 orders of magnitude. In the case of Jupiter, the H_3^+ IR and H_2 UV auroral emissions form comparable morphologies [e.g., *Clarke et al.*, 2004]. It is therefore reasonable to assume such a similarity for Saturn's aurora, with the immediate consequence that the secondary IR oval is probably reminiscent of the outer UV emission. As a corollary, the outer auroral UV emission might also result from FAC generated in the process of corotation enforcement of the lagging magnetospheric plasma. However, as demonstrated above, the energy flux of the suprathermal electrons appears to be large enough to produce the UV outer emission without field-aligned acceleration, provided the electrons are maintained in strong diffusion, and therefore the electron accel-

eration that would be related to FAC triggered by corotation enforcement process may not be required. It should be noted that this latter statement does not contradict the IR observations showing that the secondary auroral oval is associated with subcorotating plasma, but it suggests that the field-aligned current system that is generated to accelerate this plasma may play a lesser role than the precipitation of hot electrons in the production of the UV outer and secondary IR auroral emissions. A recent analysis of the magnetic field perturbations observed by Cassini in the nightside region of Saturn's high-latitude magnetosphere [*Talboys et al.*, 2009] may confirm this statement. Indeed, the authors suggest the presence of FAC mapping to 67.6°S latitude, almost exactly matching the outer auroral region. This planetward current of ~1.4 MA rad^{-1} may be associated with plasma subcorotation on outer magnetospheric lines. However, following equations (2) and (3b) of *Bunce et al.* [2008a], our 0.3 mW m^{-2} injected energy flux estimate would require that the FAC is ~50 MA rad^{-1}, assuming a 7° wide auroral emission, which is ~36 times larger than the observed value by *Talboys et al.* [2009] (we note that even with a 1° width the FAC is still 5 times larger). Neglecting possible saturation effects [*Ray et al.*, 2009] that could affect the conversion from energy flux to field-aligned current, this again implies that the FACs associated with corotation breakdown are not likely to provide enough energy flux to produce the outer auroral emission. This conclusion is compatible with the fact that the outer aurora appears to be insensitive to the solar wind conditions while the location and strength of FACs associated with corotation breakdown should respond to changes in the compression level of the magnetosphere [e.g., *Bunce et al.*, 2005].

7. Conclusions

[19] 1. The outer auroral UV emission in the southern hemisphere is a real feature revealed by limb brightening under particular HST viewing geometry.

[20] 2. It is characterized by a limb-brightening-free brightness of ~1.7 kR and an injected electron power of ~0.3 mW m^{-2} (both values are accurate within a factor of ~2).

[21] 3. Its position equatorward of the main emission (near 67°S) magnetically maps to distances in the equatorial plane from approximately 4 to 11 R_S.

[22] 4. In this region, Cassini observed a population of hot electrons, which we show is able to provide more than the energy flux that is necessary to sustain the outer auroral emission in both hemispheres without the need for field-aligned acceleration.

[23] 5. The outer emission may be directly or indirectly associated with ENAs originating from the energetic protons and O^+ distributions in the same region.

[24] 6. This UV emission might also be in accordance with the secondary IR oval linked to subcorotating magnetospheric plasma, even though the precipitating energy flux that is driven by the field-aligned current system accelerating this plasma is too small compared to the required value.

[25] **Acknowledgments.** The authors wish to thank Stan Cowley for his helpful advice. This work is based on observations with the NASA/ESA Hubble Space Telescope, obtained at the Space Telescope Science Institute (STScI), which is operated by AURA, Inc., for NASA under contract NAS5–26555. D.G., B.B., J.C.G., and A.R. are supported by the Belgian Fund for Scientific Research (F.R.S.-FNRS) and by the PRODEX Program managed by the European Space Agency in collaboration with the Belgian Federal Science Policy Office. The authors would like to thank the reviewers for their constructive suggestions on the original manuscript.

[26] Amitava Bhattacharjee thanks Emma Bunce and another reviewer for their assistance in evaluating this paper.

References

Bunce, E. J., J. D. Nichols, and S. W. H. Cowley (2005), Solar wind-magnetosphere-ionosphere coupling at Jupiter, *Adv. Space Res.*, *36*, 2090–2099, doi:10.1016/j.asr.2005.04.016.

Bunce, E. J., et al. (2008a), Origin of Saturn's aurora: Simultaneous observations by Cassini and the Hubble Space Telescope, *J. Geophys. Res.*, *113*, A09209, doi:10.1029/2008JA013257.

Bunce, E. J., C. S. Arridge, S. W. H. Cowley, and M. K. Dougherty (2008b), Magnetic field structure of Saturn's dayside magnetosphere and its mapping to the ionosphere: Results from ring current modeling, *J. Geophys. Res.*, *113*, A02207, doi:10.1029/2007JA012538.

Carbary, J. F., D. G. Mitchell, P. Brandt, E. C. Roelof, and S. M. Krimigis (2008), Statistical morphology of ENA emissions at Saturn, *J. Geophys. Res.*, *113*, A05210, doi:10.1029/2007JA012873.

Clarke, J. T., D. Grodent, S. Cowley, E. Bunce, P. Zarka, J. Connerney, and T. Satoh (2004), Jupiter's aurora, in *Jupiter: The Planet, Satellites and Magnetosphere*, edited by F. Bagenal, B. McKinnon, and T. Dowling, pp. 639–670, Cambridge Univ. Press, New York.

Clarke, J. T., et al. (2005), Morphological differences between Saturn's ultraviolet aurorae and those of Earth and Jupiter, *Nature*, *433*, 717–719, doi:10.1038/nature03331.

Clarke, J. T., et al. (2009), Response of Jupiter's and Saturn's auroral activity to the solar wind, *J. Geophys. Res.*, *114*, A05210, doi:10.1029/2008JA013694.

Cowley, S. W. H., and E. J. Bunce (2003), Corotation-driven magnetosphere-ionosphere coupling currents in Saturn's magnetosphere and their relation to the auroras, *Ann. Geophys.*, *21*, 1691–1707.

Cowley, S. W. H., E. J. Bunce, and J. M. O'Rourke (2004), A simple quantitative model of plasma flows and currents in Saturn's polar ionosphere, *J. Geophys. Res.*, *109*, A05212, doi:10.1029/2003JA010375.

Cowley, S. W. H., S. V. Badman, E. J. Bunce, J. T. Clarke, J.-C. Gérard, D. Grodent, C. M. Jackman, S. E. Milan, and T. K. Yeoman (2005), Reconnection in a rotation-dominated magnetosphere and its relation to Saturn's auroral dynamics, *J. Geophys. Res.*, *110*, A02201, doi:10.1029/2004JA010796.

Crary, F. J., et al. (2005), Solar wind dynamic pressure and electric field as the main factors controlling Saturn's aurorae, *Nature*, *433*, 720–722, doi:10.1038/nature03333.

Gérard, J.-C., B. Bonfond, J. Gustin, D. Grodent, J. T. Clarke, D. Bisikalo, and V. Shematovich (2009), Altitude of Saturn's aurora and its implications for the characteristic energy of precipitated electrons, *Geophys. Res. Lett.*, *36*, L02202, doi:10.1029/2008GL036554.

Grodent, D., G. R. Gladstone, J.-C. Gérard, V. Dols, and J. H. Waite (1997), Simulation of the morphology of the Jovian UV aurora observed with the Hubble Space Telescope, *Icarus*, *128*, 306–321, doi:10.1006/icar.1997.5740.

Grodent, D., J. H. Waite Jr., and J.-C. Gérard (2001), A self-consistent model of the Jovian auroral thermal structure, *J. Geophys. Res.*, *106*, 12,933–12,952, doi:10.1029/2000JA900129.

Grodent, D., J.-C. Gérard, S. W. H. Cowley, E. J. Bunce, and J. T. Clarke (2005), Variable morphology of Saturn's southern ultraviolet aurora, *J. Geophys. Res.*, *110*, A07215, doi:10.1029/2004JA010983.

Gustin, J., J.-C. Gérard, W. Pryor, P. D. Feldman, D. Grodent, and G. Holsclaw (2009), Characteristics of Saturn's polar atmosphere and auroral electrons derived from HST/STIS, FUSE and Cassini/UVIS spectra, *Icarus*, *200*, 176–187, doi:10.1016/j.icarus.2008.11.013.

Hubert, B., J.-C. Gérard, D. Bisikalo, V. Shematovich, S. Solomon (2001), The role of proton precipitation in the excitation of auroral FUV emissions, *J. Geophys. Res.*, *106*, 21,475–21,494, doi:10.1029/2000JA000288.

Lewis, G. R., N. André, C. S. Arridge, A. J. Coates, L. K. Gilbert, D. R. Linder, A. M. Rymer (2008), Derivation of density and temperature from the Cassini-Huygens CAPS electron spectrometer, *Planet. Space Sci.*, *56*, 901–912, doi:10.1016/j.pss.2007.12.017.

Mitchell, D. G., et al. (2009), Recurrent energization of plasma in the midnight-to-dawn quadrant of Saturn's magnetosphere, and its relationship to auroral UV and radio emissions, *Planet. Space Sci.*, *57*, 1732–1742, doi:10.1016/j.pss.2009.04.002.

Nicholson, P. D., et al. (2008), A close look at Saturn's rings with Cassini VIMS, *Icarus*, *193*, 182–212, doi:10.1016/j.icarus.2007.08.036.

Radioti, A., A. T. Tomás, D. Grodent, J.-C. Gérard, J. Gustin, B. Bonfond, N. Krupp, J. Woch, and J. D. Menietti (2009), Equatorward diffuse auro-

ral emissions at Jupiter: Simultaneous HST and Galileo observations, *Geophys. Res. Lett.*, *36*, L07101, doi:10.1029/2009GL037857.

Ray, L. C., Y.-J. Su, R. E. Ergun, P. A. Delamere, and F. Bagenal (2009), Current-voltage relation of a centrifugally confined plasma, *J. Geophys. Res.*, *114*, A04214, doi:10.1029/2008JA013969.

Scarf, F. L., D. A. Gurnett, W. S. Kurth, and R. L. Poynter (1983), Voyager plasma wave measurements at Saturn, *J. Geophys. Res.*, *88*, 8971–8984, doi:10.1029/JA088iA11p08971.

Schippers, P., et al. (2008), Multi-instrument analysis of electron populations in Saturn's magnetosphere, *J. Geophys. Res.*, *113*, A07208, doi:10.1029/2008JA013098.

Seidelmann, P. K., et al. (2007), Report of the IAU/IAG Working Group on cartographic coordinates and rotational elements: 2006, *Celestial Mech. Dyn. Astron.*, *98*, 155–180, doi:10.1007/s10569-007-9072-y.

Sergeev, V. A., E. M. Sazhina, N. A. Tsyganenko, J. Å. Lundblad, and F. Søraas (1983), Pitch-angle scattering of energetic protons in the magnetotail current sheet as the dominant source of their isotropic precipitation into the nightside ionosphere, *J. Geophys. Res.*, *31*, 1147–1155.

Sergis, N., S. M. Krimigis, D. G. Mitchell, D. C. Hamilton, N. Krupp, B. M. Mauk, E. C. Roelof, and M. Dougherty (2007), Ring current at Saturn: Energetic particle pressure in Saturn's equatorial magnetosphere measured with Cassini/MIMI, *Geophys. Res. Lett.*, *34*, L09102, doi:10.1029/2006GL029223.

Stallard, T. S., S. Miller, H. Melin, M. Lystrup, S. W. H. Cowley, E. J. Bunce, N. Achilleos, and M. Dougherty (2008), Jovian-like aurorae on Saturn, *Nature*, *453*, 1083–1085, doi:10.1038/nature07077.

Talboys, D. L., C. S. Arridge, E. J. Bunce, A. J. Coates, S. W. H. Cowley, M. K. Dougherty, and K. K. Khurana (2009), Signatures of field-aligned currents in Saturn's nightside magnetosphere, *Geophys. Res. Lett.*, *36*, L19107, doi:10.1029/2009GL039867.

Tomás, A. T., J. Woch, N. Krupp, A. Lagg, K.-H. Glassmeier, and W. S. Kurth (2004), Energetic electrons in the inner part of the Jovian magnetosphere and their relation to auroral emissions, *J. Geophys. Res.*, *109*, A06203, doi:10.1029/2004JA010405.

Vincent, M. B., et al. (2000), Mapping Jupiter's latitudinal bands and Great Red Spot using HST/WFPC2 far-ultraviolet imaging, *Icarus*, *143*, 189–204, doi:10.1006/icar.1999.6232.

Young, D. T., et al. (2005), Composition and dynamics of plasma in Saturn's magnetosphere, *Science*, *307*, 1262–1266, doi:10.1126/science.1106151.

B. Bonfond, J.-C. Gérard, D. Grodent, and A. Radioti, LPAP, Institut d'Astrophysique et de Géophysique, Université de Liège, Allée du 6 Août, 17 (B5c), B-4000 Liège, Belgium. (d.grodent@ulg.ac.be)